Soil Dynamics and Earthquake Engineering, 2019, Vol. 124, pp. 184-196, DOI: 10.1016/j.soildyn.2019.05.002

Correlations of the liquefaction resistance of sands in spreader dumps of lignite opencast mines with CPT tip resistance and shear wave velocity

T. Wichtmann[i)] ; I. Kimmig[ii)]; K. Steller[iii)]; Th. Triantafyllidis[iv)] ; M. Back[v)] ; D. Dahmen[vi)]

Abstract: Correlations between the liquefaction resistance of sands in spreader dumps of lignite opencast mines on one side and the CPT tip resistance or the shear wave velocity on the other side have been developed based on an extensive experimental study on 10 different sands. The cyclic resistance ratio $CRR(N_f = 10)$ for a failure in 10 cycles, defined as the liquefaction resistance herein, was determined from undrained cyclic triaxial tests for all materials. The CPT tip resistance q_c was measured in soundings performed in a calibration chamber. The shear wave velocity v_S was obtained from measurements in a triaxial cell by means of bender elements. All three quantities $CRR(N_f = 10)$, q_c and v_S were determined for different relative densities D_r. In case of q_c and v_S also the pressure-dependence was examined in order to derive suitable equations for a pressure-normalization being necessary for the interpretation of field test data, giving values q_{c1} and v_{S1} for a mean effective stress of $p' = 100$ kPa. The procedure for the development of the $CRR(N_f = 10)$-q_{c1} and $CRR(N_f = 10)$-v_{S1} correlations based on the experimental data is explained. The correlations derived for the various sands in the present study are analyzed with respect to the influence of the grain size distribution curve and compared to respective relationships for natural soils or uncompacted recent artificial fills from the literature.

Keywords: sands; spreader dumps; lignite opencast mines; liquefaction resistance; undrained cyclic triaxial tests; CPT tip resistance; calibration chamber; shear wave velocity; bender elements; correlations

1 Introduction

The liquefaction resistance of a ground is often evaluated based on correlations with the CPT or SPT penetration resistance [4, 5, 9, 18, 22, 23, 26, 27, 29–32] or with the shear wave velocity [3, 9, 10, 19, 28, 34]. Examples for respective correlation diagrams are shown in Figures 1 to 3. They are showing a cyclic resistance ratio, defined as the shear stress amplitude τ^{ampl} causing a liquefaction in a certain number of cycles divided by the vertical effective stress σ'_v on the ordinate and the penetration resistance or shear wave velocity on the abscissa. Such diagrams have been developed by collecting field data from CPT or SPT (tip resistance q_c in case of CPT, blow count N_{SPT} in case of SPT) or shear wave velocity measurements (v_S). Furthermore, one needs information regarding the cyclic stress ratio CSR induced in the ground by an earthquake and whether this action has lead to a liquefaction or not. Combinations of CSR with q_c, N_{SPT} or v_S having lead to liquefaction are usually marked by filled symbols (see Figures 1 to 3), while the symbols for combinations without any visible signs of liquefaction remain empty. Finally, a bounding curve is drawn, separating the "liquefaction" from the "no liquefaction" cases. These bounding curves sometimes consider further parameters like fines content or mean grain size. They are usually established for a certain earthquake magnitude M_W. Curves for other magnitudes can be obtained by multiplication with a correction factor MSF. However, almost all such correlations proposed in the literature are valid for natural soils only (see Figures 1 and 2). A first CSR-v_S correlation diagram for uncompacted recent artificial fills has been recently proposed by Dobry et al. [10] (Figure 3). No correlations for an estimation of the liquefaction resistance of such fills based on CPT or SPT field data exist so far.

The experimental study presented in this paper is part of an ongoing research done in the laboratory of the Institute of Soil Mechanics and Rock Mechanics (IBF) at Karlsruhe Institute of Technology (KIT). This research is dedicated to the soils deposited in the dumps of the opencast mines in the Rhenish lignite-mining area. After the depletion of the mines in several years to decades, the remaining holes of the currently three active mines will be recultivated as lakes. The deposited soils in the dumps will then form the embankment of these lakes. Since the Rhenish lignite-mining area lies in a region with seismic activity the liquefaction resistance of the deposited soils is of interest. The maximum moment magnitude M_W of earthquakes in the Lower Rhine Embayment based on palaeoseismic and tectonic studies has been estimated to 6.8-7.0 (e.g. [2, 12, 13]). Such strong earthquakes have return periods of several thousand years. Despite the existence of to date 57 mining lakes in this region, there was only one minor local effect of slope defor-

[i)] Professor for Geotechnical Engineering, Bauhaus-Universität Weimar, Germany (corresponding author). Email: torsten.wichtmann@uni-weimar.de

[ii)] Researcher, Institute of Soil Mechanics and Rock Mechanics, Karlsruhe Institute of Technology, Germany

[iii)] Researcher, Institute of Soil Mechanics and Rock Mechanics, Karlsruhe Institute of Technology, Germany

[iv)] Professor and Director of the Institute of Soil Mechanics and Rock Mechanics, Karlsruhe Institute of Technology, Germany

[v)] RWE Power AG, Bergheim, Germany

[vi)] RWE Power AG, Bergheim, Germany

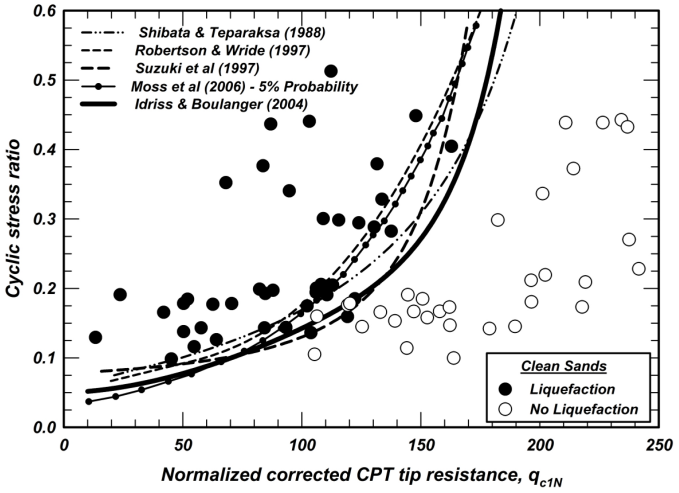

Fig. 1: *Correlation between the liquefaction resistance of natural soils and the CPT tip resistance for an earthquake of magnitude $M_W = 7.5$ (Idriss & Boulanger [5, 15, 16]). The values on the abscissa are given in the unit [0.1 MPa].*

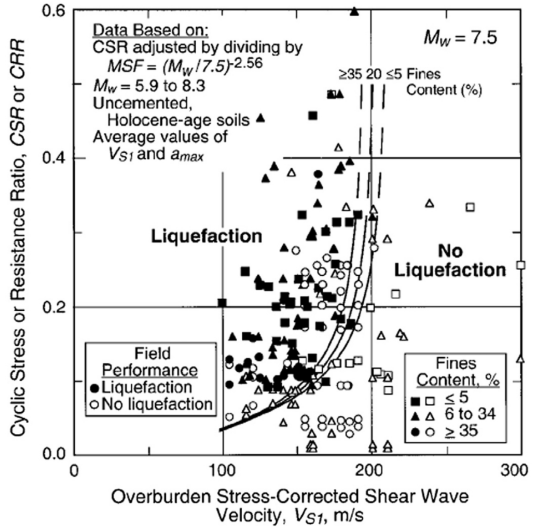

Fig. 2: *Correlation between the liquefaction resistance of natural soils and the shear wave velocity for $M_W = 7.5$ (Andrus & Stokoe [3])*

mation, induced by the 1992 Roermond earthquake (M_W = 5.4, [7]) which was obviously not caused by liquefaction [25]. However, the embankments of the presently planned mining lakes are designed for the ground motion of an M_W = 6 earthquake with a typical number of equivalent cycles of $N_{eq} = 10$ and the corresponding distance from the epicenter of 5 km.

For an evaluation of the liquefaction resistance of the sands in the spreader dumps based on CPT or shear wave velocity field data, suitable correlation diagrams are needed. The applicability of the available correlations for natural soils to these artificial fills cannot be presumed in view of the significant differences in fabric resulting from the deposition process (see [35] for details). Therefore, specific correlation diagrams for the sands in the spreader dumps have to be established. In contrast to the diagrams in Figures 1 to 3 these new correlations cannot be based

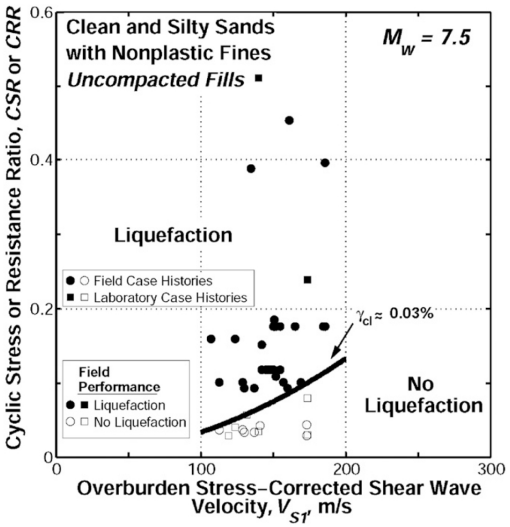

Fig. 3: *Correlation between the liquefaction resistance of uncompacted recent artificial fills and the shear wave velocity for $M_W = 7.5$ (Dobry et al. [10])*

on $CSR \leftrightarrow q_c$ or $CSR \leftrightarrow v_S$ field data, because such data do not exist since the embankments have not been formed yet. The sands in the dumps of the three active mines in the Rhenish lignite-mining area are currently in a partially saturated state. Collecting $CSR \leftrightarrow q_c$ or $CSR \leftrightarrow v_S$ field data for correlation diagrams requires a water-saturation of the sands, however, and the occurrence of several earthquakes of different magnitudes to collect a sufficient amount of data for the correlations. Therefore, in order to judge the liquefaction resistance of the dumps before flooding of the lakes, another procedure had to be chosen for the development of the correlation diagrams. The new diagrams are based on an extensive laboratory study, involving undrained cyclic triaxial tests, CPT data in a calibration chamber and shear wave velocity measurements. Several typical sands from the spreader dumps have been considered in the study.

A parametric study on the liquefaction resistance with numerous undrained cyclic triaxial tests performed on various soils from the dumps in the Rhenish lignite-mining area is documented in [35]. Field tests with the aim to determine the relative density in the dumps are also described in [35]. Typical CPT data from a dump in the Rhenish lignite-mining area, showing rather small values of tip resistance q_c, are provided in Figure 4.

2 Tested materials

Ten materials were involved in the present study. Eight of them were sampled in the spreader dumps of the opencast mines in the Rhenish lignite-mining area. The nomination of these sands has been overtaken from [35], see Table 1. Two standard sands of the IBF, named C1 and C2, were also included in the program. The grain size distribution curves of all tested materials are summarized in Figure 5. They encompass the whole bandwidth of granular soils typically encountered in the dumps of the opencast mines under consideration. The parameters of the test materials are provided in Table 1. The fines content FC of the soils from the dumps consists of low to highly plastic clays.

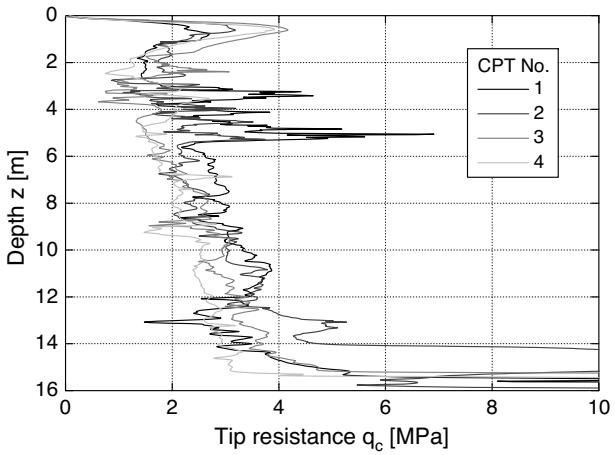

Fig. 4: *Example of CPT data from a dump in the Rhenish lignite-mining area*

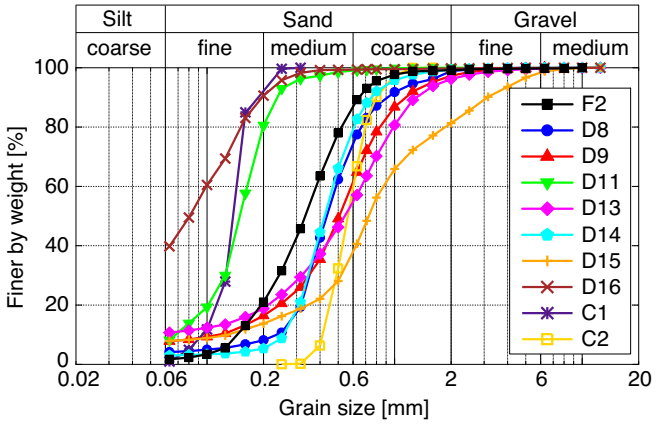

Fig. 5: *Grain size distribution curves of the tested materials*

Mat.	FC [%]	d_{50} [mm]	C_u [-]	ϱ_s [g/cm^3]	$\varrho_{d,\min}$ [g/cm^3]	$\varrho_{d,\max}$ [g/cm^3]	$e_{\min}$ [-]	$e_{\max}$ [-]
F2	1.7	0.33	2.6	2.64	1.387	1.727	0.529	0.903
D8	4.2	0.43	2.1	2.63	1.413	1.682	0.564	0.861
D9	7.8	0.51	5.1	2.64	1.428	1.776	0.486	0.849
D11	8.2	0.15	2.4	2.64	1.245	1.631	0.619	1.120
D13	10.7	0.54	3.8	2.64	1.419	1.789	0.476	0.860
D14	3.0	0.42	1.8	2.64	1.431	1.699	0.554	0.845
D15	7.9	0.73	6.8	2.64	1.607	1.922	0.374	0.643
D16	39.8	0.08	-	2.62	1.283	1.698	0.543	1.042
C1	0.9	0.14	1.5	2.65	1.290	1.580	0.677	1.054
C2	0	0.56	1.5	2.64	1.427	1.705	0.548	0.850

Table 1: Fines content FC (grain sizes < 0.063 mm according to German standard code [**?**]), mean grain size d_{50}, uniformity coefficient $C_u = d_{60}/d_{10}$, grain density ϱ_s, minimum and maximum dry densities $\varrho_{d,\min}$ and $\varrho_{d,\max}$ and minimum and maximum void ratios $e_{\min}$ and $e_{\max}$ of the tested materials. In case of a fines content 10 % $\leq FC \leq$ 20 %, the uniformity coefficient was evaluated as $C_u^* = d_{70}/d_{20}$ due to missing information regarding the grain size distribution curve in the range $d < 0.063$ mm.

3 Undrained cyclic triaxial tests

The procedure of the undrained cyclic triaxial tests was identical to that explained in detail in [35]. All samples measured 10 cm in diameter and 10 cm in height. Parts of the samples were prepared by a special method developed to reproduce the deposition process in the spreader dumps and thus the initial fabric generated by this process. In this "free fall" method (see also [35]) the moist sand falls out of a certain height (usually 1.5 m) in the split mould. Different initial densities were achieved by varying the water content during preparation. The maximum relative densities that can be achieved by this method are limited, however, depending on the grain size distribution of the test material. In order to reach higher densities than those reported in [35], additional samples were prepared by moist tamping in eight layers using a degree of undercompaction of 10 % according to Ladd [20]. After preparation, all samples were fully saturated with demineralized deaerated water using a back pressure of 500 kPa, consolidated isotropically under a mean effective stress of $p'_0 = 100$ kPa and then subjected to an undrained cyclic loading till failure. Failure was defined as reaching an axial strain of $|\varepsilon_1| = 10$ % during either compression or extension. Beside the variation of density, each material was tested under various amplitudes of cyclic loading.

Typical test results for sands from the spreader dumps are presented in [35]. Figure 6 collects the results of all tests performed in the present study, in diagrams giving the cyclic stress ratio $CSR = q^{\text{ampl}}/(2p'_0)$ as a function of the number of cycles to failure. Each data point belongs to a single test. The relative density $D_r = (e_{\max} - e)/(e_{\max} - e_{\min})$ of the respective test, measured after the closure of the drainage lines, is given beside the data points. Points with similar densities are fitted with curves. The average density of the respective tests is given beside the curves. The diagrams in Figure 6 show the well-known increase of the applicable number of cycles with a reduction in amplitude and an increase in density. The liquefaction resistance $CRR(N_f = 10)$ (cyclic resistance ratio) was read out of the diagrams in Figure 6, on the curves for the different D_r values, as the cyclic stress ratio causing failure in $N_f = 10$ cycles. The number of cycles $N_f = 10$ was chosen because it is typical for an earthquake in the Rhenish lignite-mining area.

In Figure 7 the $CRR(N_f = 10)$ values are given as a function of relative density D_{r0} for all tested materials. The linear relationship between $CRR(N_f = 10)$ and D_r reported for the soils from the dumps in [35] is confirmed by the data in Figure 7 even at the higher relative densities tested in the present study. Although the $CRR(N_f = 10)$-D_r data of some of the soils (e.g. C1, D14) could be approximated even slightly better by nonlinear curves, linear functions are regarded as sufficient in the range of tested densities. The quality of the fit can be judged based on the adjusted R-square values R^2 given in the legend of Figure 7 (obtained with program Origin). A sharp increase of $CRR(N_f = 10)$ at larger densities, as it is sometimes reported in the literature [33], has not been observed for the soils from the dumps within the tested D_r range. In Figure 7, for a given relative density, the lowest liquefaction resistance is observed for the material D16 having the highest fines content. The largest $CRR(N_f = 10)$ values were obtained for the clean medium coarse sand C2.

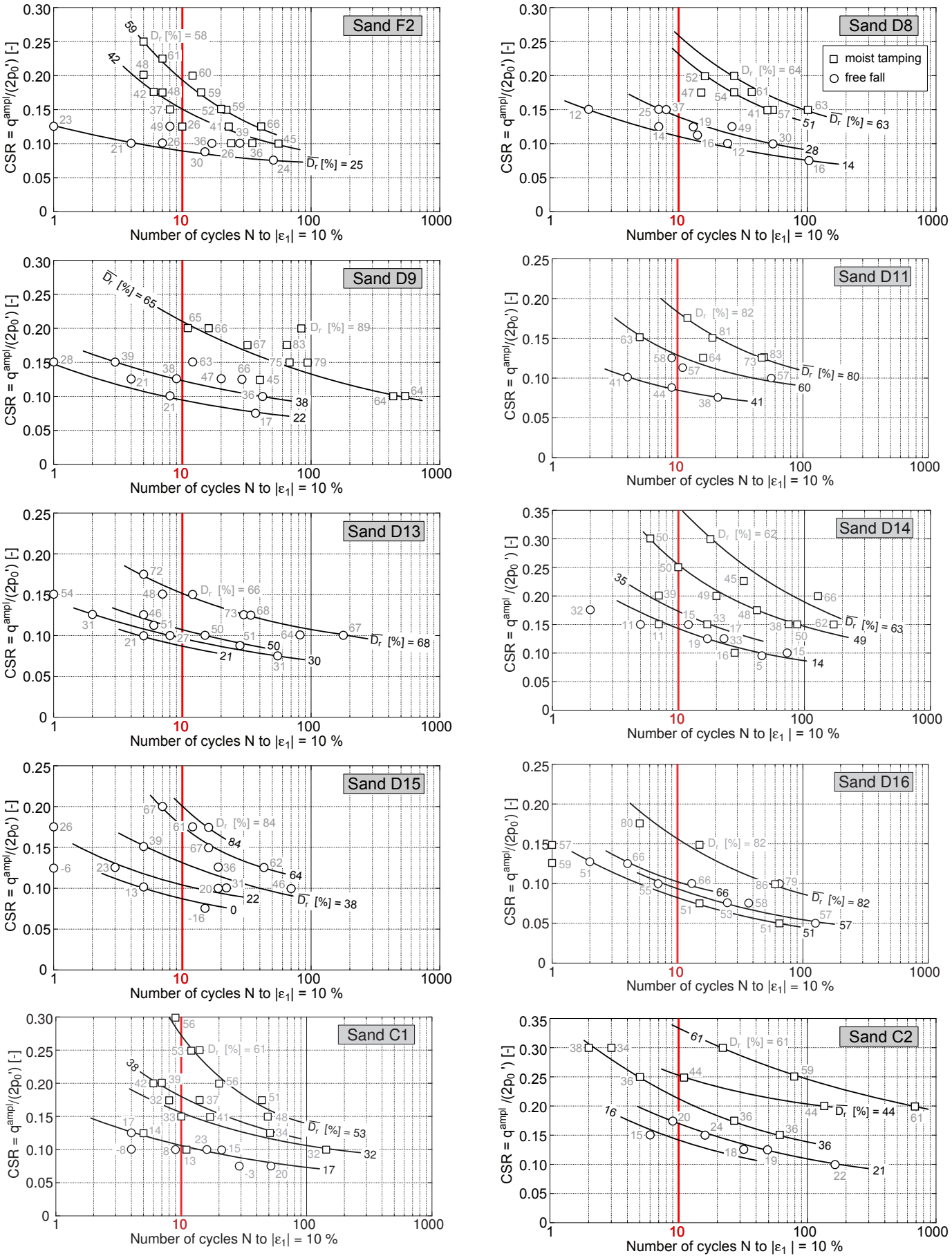

Fig. 6: Cyclic stress ratio $CSR = q^{\mathrm{ampl}}/(2p_0')$ as a function of the number of cycles to failure for all tested materials obtained from undrained cyclic triaxial tests

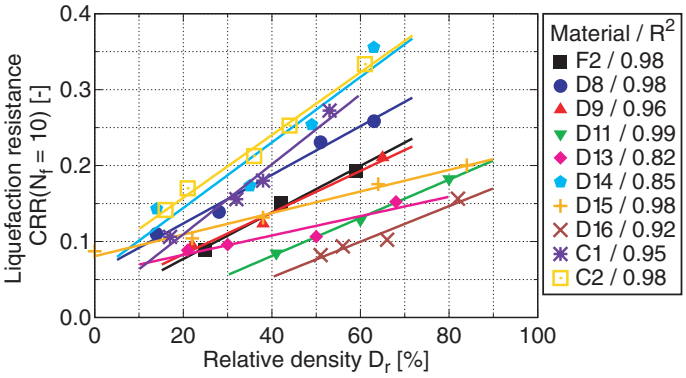

Fig. 7: *Liquefaction resistance $CRR(N_f = 10)$ in dependence of relative density D_r for all tested materials*

The dependencies between the liquefaction resistance and the parameters of the grain size distribution curve can be judged based on Figure 8. It shows data for two different relative densities, D_r = 30 % and 60 %. The data for D_r = 30 % are the same as analyzed in [35], but supplemented by the results for material D16 (the $CRR(D_r)$ curve for D16 in Figure 7 had to be extrapolated to D_r = 30 %) and restricted to the ten soils considered in the present paper. In contrast to [35] the additional tests on samples prepared by moist tamping allow the analysis of the dependencies at a higher relative density, i.e. at D_r = 60 %. The decrease of the liquefaction resistance with increasing plastic fines content known from [35] for D_r = 30 % is visible also in the reduced data set in Figure 8a. It is even more pronounced in the present study due to the additional data for D16 having a high fines content of almost 40 %. The rise of $CRR(N_f = 10)$ with increasing mean grain size d_{50} is more evident in the data set for D_r = 30 % (Figure 8b) than for D_r = 60 % (Figure 8e). Neglecting the single data point for sand D11, Figures 8c and 8f give hints for a reduction of the liquefaction resistance with growing uniformity coefficient C_u. The data set for a larger number of materials analyzed in [35], however, allowed no final conclusion regarding a possible C_u dependence of $CRR(N_f = 10)$. A comparison of the observed tendencies with the literature is undertaken in [35].

4 CPT soundings in the calibration chamber

A scheme of the calibration chamber for CPT at the IBF is shown in Figure 9. It allows testing of cylindrical samples with a diameter of 1 m and a height of 1.5 m. The lateral boundary of the cell and the bottom and top plates are equipped with membranes. By applying an air pressure to these membranes the sample can be set under an isotropic or anisotropic state of stress. Only isotropic stress conditions were tested in the present study so far. The maximum pressure applicable to the membranes is 300 kPa. The top plate includes a central hole with a vertical guidance through which a standard CPT probe (the same as used in field testing) can be pushed into the sample up to a depth of about 1.2 m. The tests were realized with a constant penetration velocity of 16 mm/s by means of a hydraulic system.

All samples were prepared by moist tamping in 15 layers each having a thickness of about 10 cm. The water contents lay in the range 5 % $\leq w \leq$ 15 % (in detail: 5.8 % $\leq w \leq$ 11.2 % for D13, 7.3 % $\leq w \leq$ 8.5 % for D14, 6.6 % $\leq w \leq$ 11.4 % for D15 and 5.4 % $\leq w \leq$ 14.7 % for D16), corresponding to degrees of saturation in the range 22.7 % $\leq S_r \leq$ 55.7 % (in detail: 22.7 % $\leq S_r \leq$ 48.0 % for D13, 29.5 % $\leq S_r \leq$ 35.7 % for D14, 29.9 % $\leq S_r \leq$ 55.7 % for D15 and 24.2 % $\leq S_r \leq$ 54.1 % for D16). The tests in the calibration chamber were performed on partially saturated samples, because the CPT in the spreader dumps, which will be used as the basis for the evaluation of the liquefaction resistance, will be performed before flooding of the lakes. It should be mentioned that even after flooding the soils in the dumps will probably not have reached a fully water-saturated state (see the test series on the influence of the degree of saturation in [35]). The range of water contents chosen in the calibration chamber tests agrees well with the range encountered in the dumps in field tests. The field tests revealed that sands with higher plastic fines contents usually possess a higher water content.

After completion of a test, the local distribution of relative density in the large sample was determined by taking subsamples by means of thin-walled stainless steel tubes measuring 150 mm in diameter and 170 mm in height (Figure 10). The samples were taken in four different depths, in a distance of about 250 mm from the center of the calibration chamber. In the upper three depths three samples per layer were taken equally distributed over the cross-section. In the lowest layer only two samples could be taken, because a person had to enter the chamber for sampling. Unfortunately, no direct information of the local relative density in the central part of the sample, i.e. in the line of sounding can be obtained, since the soil is disturbed (compacted) there as a result of the sounding. The average value of all tube samples of a certain layer is set into approach as the relative density of that layer.

A typical result of a CPT in the calibration chamber is shown in Figure 11. It has been obtained for the material D14 in a test with a pressure p = 100 kPa. Figure 11a presents the development of the tip resistance q_c with depth z. The strong initial increase of q_c up to a depth of 0.2 m is caused by the penetration of the CPT probe into the sample. The tip resistance remains almost constant during further penetration, showing a very small reduction with depth only. The course of shaft friction f_s with depth resembles that of q_c (Figure 11b), leading to a rather constant friction ratio of $R_f = f_s/q_c \approx 0.4$ % (Figure 11c), which lies in the range of typical values for sand. Figure 11d presents the variation of relative density D_r with depth, evaluated based on the subsamples taken during the dismantling of the sample. The filled circular symbols represent the D_r values of the individual tubes, while the continuous line connects the average D_r values calculated for each depth. The relative density shows a slight decrease with depth, which is the reason for the similar tendencies in the curves $q_c(z)$ and $f_s(z)$. The water content w determined based on the tube samples is shown in a similar representation in Figure 11e. It is almost constant in the whole sample. For each layer of tube samples an average value of the tip resistance q_c was determined, shown as the filled circular symbols in Figure 11a. The averaging of the $q_c(z)$ curve was undertaken over the height of the tube sample (170 mm).

A correction of the values $q_c = q_{c,Chamber}$ measured in the calibration chamber tests by a factor K_{cc} in order to convert them to values $q_{c,Field}$ to be expected in the field

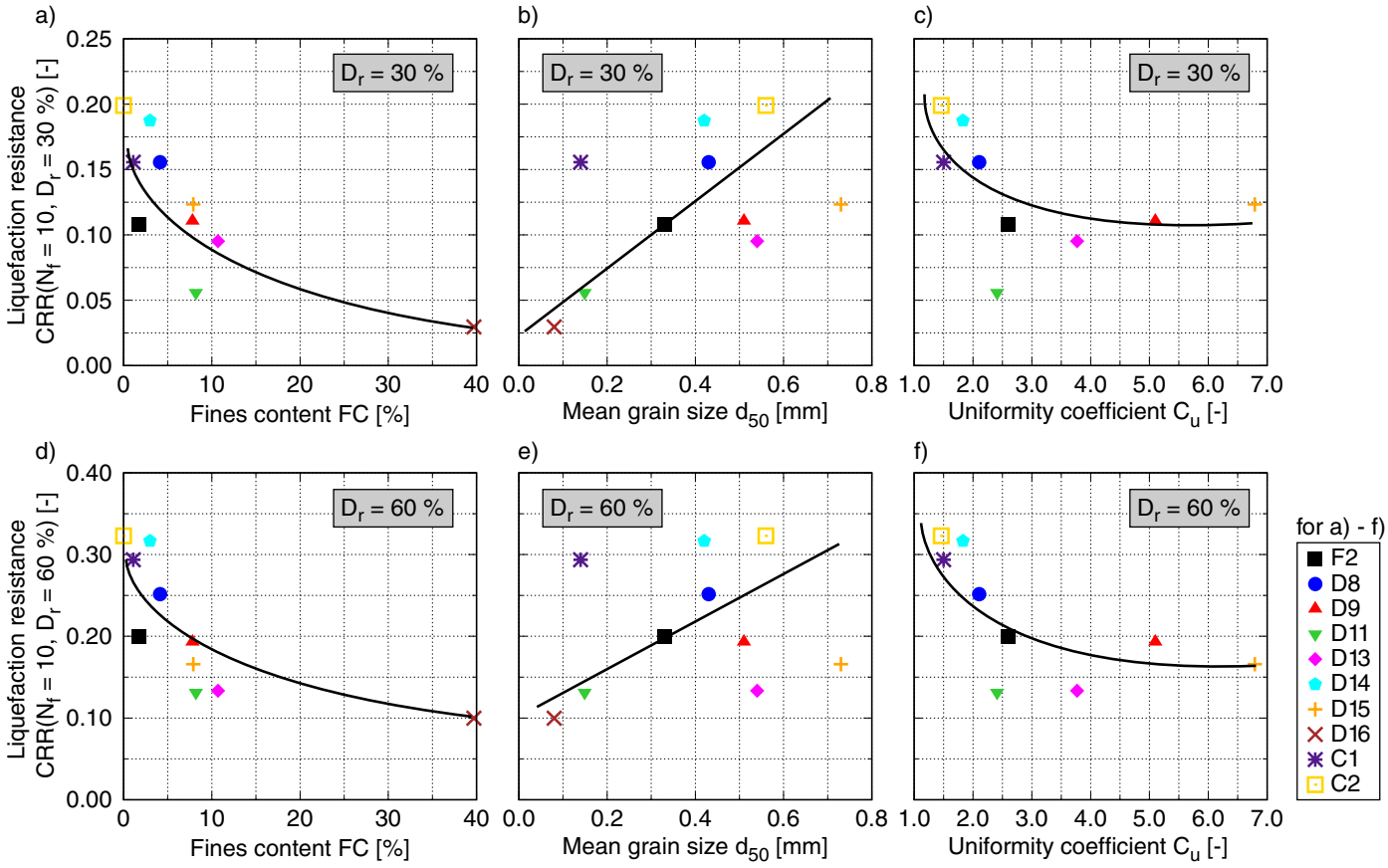

Fig. 8: *Liquefaction resistance $CRR(N_f = 10)$ from undrained cyclic triaxial tests for a-c) $D_r = 30$ % and d-f) $D_r = 60$ % in dependence of fines content FC, mean grain size d_{50} and uniformity coefficient C_u*

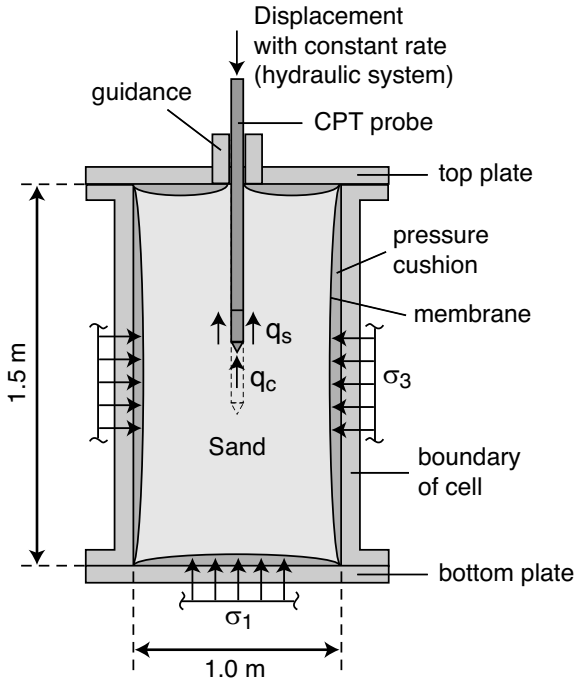

Fig. 9: *Scheme of the calibration chamber at the IBF*

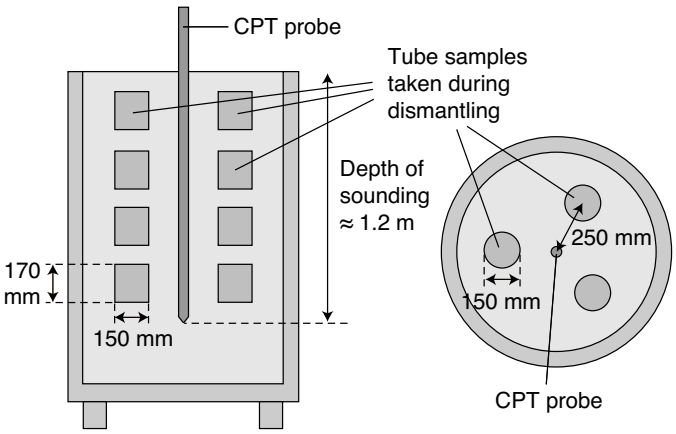

Fig. 10: *Positions of the subsamples taken during the dismantling of the sample after completion of a test in the calibration chamber*

is not undertaken in this paper. It is unclear so far if the available correction functions in the literature, e.g. the one proposed by Mayne & Kulhawy [21]

$$K_{cc} = \left(\frac{\eta - A}{\eta_0}\right)^{-D_r/B} \quad (1)$$

with the ratio $\eta = D_c/d_c$ of the diameters of the calibration chamber (D_c) and the CPT probe (d_c) and three parameters A, B and η_0, are applicable to the rather loose soils

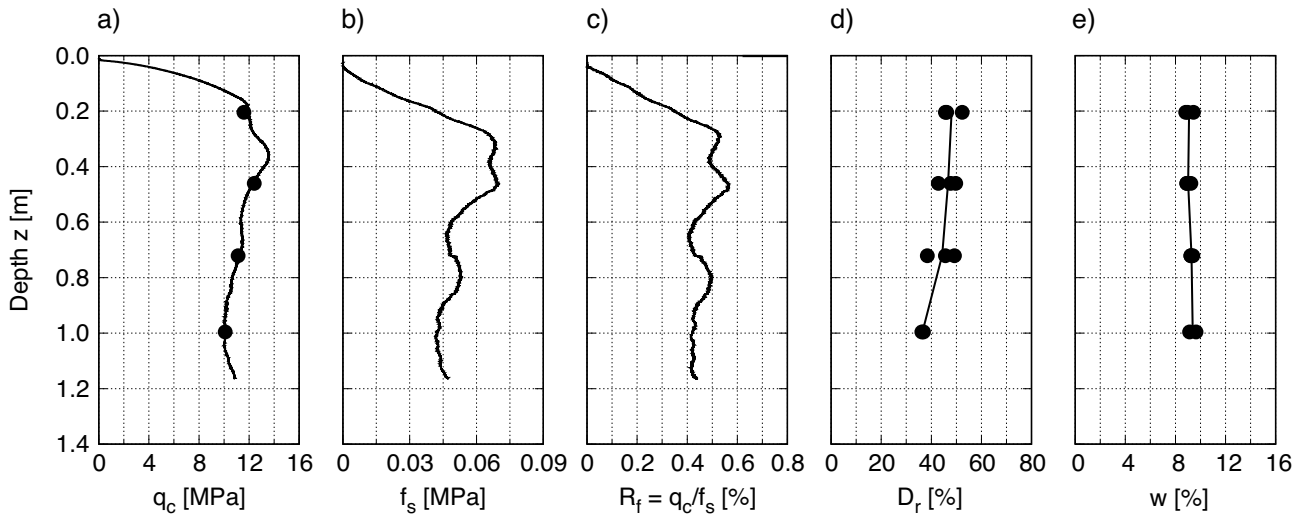

Fig. 11: *Typical results of a test in the calibration chamber (material D14, pressure $p = 100$ kPa): a) tip resistance $q_c(z)$, b) shaft friction $f_s(z)$, c) friction ratio $R_f(z) = f_s(z)/q_c(z)$, d) relative density $D_r(z)$ and e) water content $w(z)$ derived from the subsamples*

from the dumps. For orientation, with the diameters $D_c = 1.0$ m and $d_c = 36$ mm of the applied equipment and assuming $A = 0$ and $\eta_0 = 60$ (similar to [8]), Eq. (1) delivers values of the correction factor K_{cc} between 1.05 (for loose sand and $B = 1$) and 2.0 (for dense sand and $B = 4$). The development of a suitable K_{cc} factor for the soils from the dumps is planned for the future, based on CPT in calibration chambers which different sample diameters. In the following, the q_c values measured in the calibration chamber are presented and further analysed without applying such correction.

Due to the large effort for a single test, only four of the ten materials introduced in Section 2 have been tested in the calibration chamber so far, namely the sands D13 to D16. In a first series of tests, for each soil several samples having different densities were tested at a pressure $p = 100$ kPa. In a second test series performed on each soil, the pressure was varied between 0 and 300 kPa in steps of 25 or 50 kPa. In this second series all samples had a similar density. For each combination of density and pressure a new sample was prepared. Preliminary multi-stage tests in which different pressures were applied in succession have been proven as unfeasible.

Figure 12 presents the results of the first test series performed with a variation of density and a constant pressure $p = 100$ kPa. The average q_c values (filled circular symbols in Figure 11a) are plotted versus the corresponding average D_r values (connected by the line in Figure 11d). Only the data of the three lower layers of tube samples taken at depths 0.4 m $\leq z \leq$ 1.2 m have been considered in Figure 12. The data of the uppermost layer ($z \approx 0.2$ m) has been omitted since it may be falsified by boundary effects, in view of its vicinity to the point of entrance of the CPT probe. For all four tested materials, the data in Figure 12 show an overproportional increase of the tip resistance with increasing relative density. Obviously, for a certain D_r, the q_c values of the materials D13 and D16 lie significantly below those of D14 and D15. This may be a consequence of the higher plastic fines content of these materials (D13: $FC = 10.7$ %, D16: $FC = 39.8$ %). The scatter of data for the material D15 is larger than for all other tested soils, probably because of its larger content of gravelly particles. For comparison, the $q_c(D_r)$ relationships provided in German standard code DIN 4094-1 [1] for natural granular soils, in particular uniformly graded sands and sand-gravel mixtures, have been added to Figure 12. The data of the present test series shows some discrepancies from the DIN curves, revealing that the dependence of the $q_c(D_r)$ relationship on the grain size distribution curve is somewhat more complex for the sands in the spreader dumps. Further research with additional tests on other materials from the dumps is necessary to work out this dependence more clearly.

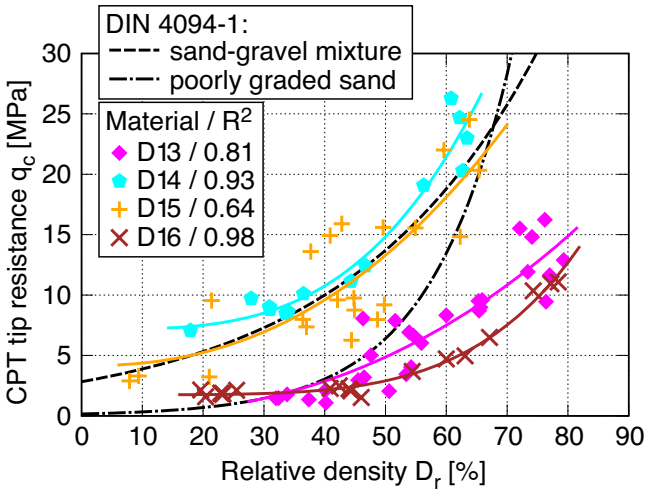

Fig. 12: *CPT tip resistance q_c for a pressure $p = 100$ kPa versus relative density D_r for all tested materials*

The pressure-dependence of q_c is inspected in Figure 13, based on the data from the second test series with a variation of p at almost constant density for a certain soil. When calculating the mean stress from $p = (\sigma_1 + 2\sigma_3)/3$ the vertical stress $\sigma_{1,0}$ in the middle of the sample resulting from the self-weight of the sample has been considered. The corresponding portion of radial stress is estimated from $\sigma_{3,0} = K_0\ \sigma_{1,0}$ with $K_0 = 0.5$. The portion of mean stress resulting from the self-weight of the soil sample amounts

$p_0 \approx 10$ kPa. The state of stress caused by the self-weight is superposed by the isotropic stress applied via the membranes of the calibration chamber. The ranges of relative densities obtained from the tube samples in this test series, which are inevitable despite constant target density, are given in the legend of Figure 13. They were somewhat different for the four tested materials. The scatter of data in Figure 13 mainly results from variations in density, and is again larger for the coarsest material D15. Despite that scatter an underproportional increase of the tip resistance with pressure is evident in Figure 13 for all four tested materials.

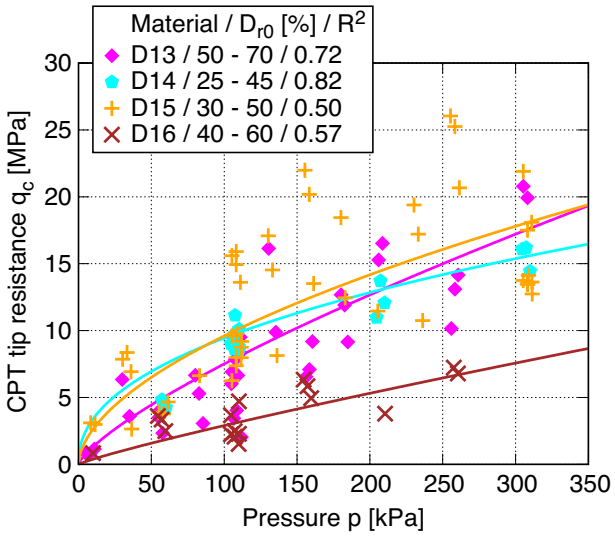

Fig. 13: *CPT tip resistance q_c versus pressure p from tests with different pressures but similar relative densities for a given material*

In order to evaluate CPT field test data with respect to the liquefaction resistance, the tip resistance q_c measured in a certain depth and thus at a certain vertical effective stress σ'_v is converted to a value q_{c1} at a certain reference stress $\sigma'_v = 98$ or 100 kPa [17, 28, 29, 31]:

$$q_{c1} = C_{qc}\, q_c \tag{2}$$

In order to derive a suitable correction factor C_{qc}, the data in Figure 13 have been further analyzed in Figure 14. First, the scatter has been reduced by converting the measured data to q_c values for the average relative density $\overline{D_r}$ of the tests performed on a certain material, using the curves $q_c(D_r)$ shown in Figure 12. The average values $\overline{D_r}$ are given in the legend of Figure 14. In a second step, the q_c data were divided by q_{c1}, which is defined as the q_c value at the reference pressure $p = 100$ kPa. Note that $\sigma'_v \approx p' = p$ holds for the tests of the present study with their almost isotropic stress conditions. Despite the large scatter of data in Figure 14 a curve-fitting was undertaken using the following function

$$\frac{q_c}{q_{c1}} = \frac{1}{C_{qc}} = \left(\frac{p}{100}\right)^c \tag{3}$$

delivering a constant $c = 0.59$ (see solid curve in Figure 14).

It should be kept in mind that the pressure-dependence of q_c has been studied for a narrow range of relative densities only. Therefore, the application of Eq. (3) to lower or higher relative densities could lead to some error, which cannot be quantified yet. However, usually no D_r dependence is considered in formulas like (3) proposed in the literature [17, 28, 29, 31].

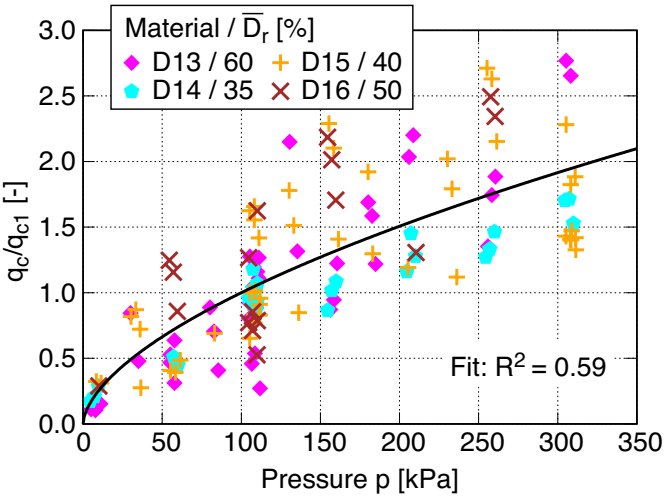

Fig. 14: *CPT tip resistance q_c converted to a value for the average soil density $\overline{D_r}$ given in the legend and divided by q_{c1}. Tip resistance q_{c1} is evaluated as the q_c value at $\overline{D_r}$ and $p = 100$ kPa*

5 Correlation between CPT tip resistance and liquefaction resistance

The procedure for the development of a correlation between the CPT tip resistance measured in the calibration chamber and the liquefaction resistance $CRR(N_f = 10)$ derived from the undrained cyclic triaxial tests is shown in Figure 15, based on the data for the sand D13. Figure 15a repeats the relationship between $CRR(N_f = 10)$ and relative density D_r for $p'_0 = 100$ kPa from Figure 7, while Figure 15c contains the q_{c1}-D_r relationship from Figure 12, but shown with reversed axes. Since all tests in Figure 12 have been performed with $p = 100$ kPa, $q_{c1} = q_c$ holds for this data set. For certain values of relative density D_r, the corresponding values of $CRR(N_f = 10)$ and q_{c1} are taken from the diagrams in Figures 15a and 15c and plotted against each other in the $CRR(N_f = 10)$-q_{c1} diagram provided in Figure 15b. The points for different D_r values are connected forming the correlation between $CRR(N_f = 10)$ and q_{c1}. In this case, $CRR(N_f = 10)$ grows somewhat underproportional with q_{c1}.

Note that the relative density $D_r = (e_{max} - e)/(e_{max} - e_{min})$ is evaluated with constant values of e_{max} and e_{min} determined from standard laboratory tests at zero pressure ($p = 0$) in this study. An application of an alternative definition of D_r, using pressure-dependent e_{max} and e_{min} values derived from oedometric or isotropic compression tests [24], would not change the correlation curve in Figure 15b. This is due to the fact that D_r is only an auxiliary quantity in the development of the correlation curve, used to read data from both types of test at the same state, i.e. at same D_r.

The $CRR(N_f = 10)$-q_{c1} correlations derived for the four soils D13 - D16 are collected in Figure 16. For comparison the relationships for natural sands from Figure 1 have been added. Evidently, the curves for the three materials D13, D15 and D16 lay in a similar range, while the lique-

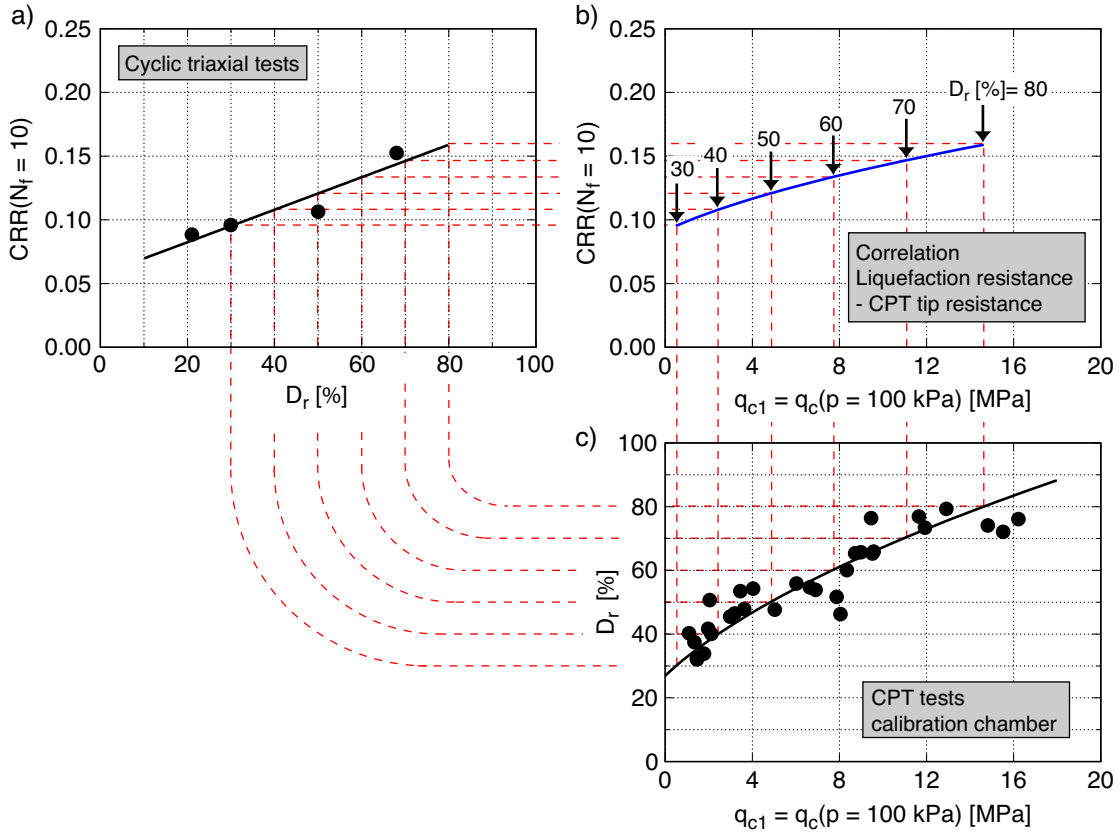

Fig. 15: *Development of the correlation diagram between CPT tip resistance q_{c1} for $p = 100$ kPa and liquefaction resistance $CRR(N_f = 10)$ for material D13*

faction resistance for D14 is considerably higher at a given CPT tip resistance. Compared to the other three materials, D14 possesses a lower fines content and its grading is more uniform. If this is the reason for the deviating $CRR(N_f = 10)$-q_{c1} relationship has to be clarified in future based on additional tests on other clean uniform sands (e.g. C1 and C2, Table 1). The $CRR(N_f = 10)$-q_{c1} correlations for the sands from the spreader dumps run flatter than the relationships for natural sands from the literature. Furthermore, they show an underproportional increase of $CRR(N_f = 10)$ with q_{c1}, at least in the range of tested densities, while the published relationships for natural soils reveal the opposite trend, i.e. a strongly overproportional increase of CRR at higher values of tip resistance. Typical values of the pressure-normalized tip resistance q_{c1} in the spreader dumps of the Rhenish lignite-mining area lie between 2 and 10 MPa (compare Figure 4). In that range the liquefaction resistance $CRR(N_f = 10)$ derived from the novel correlations is somewhat larger than that obtained from the correlations proposed in the literature for natural soils. An application of correction factors K_{cc}, in order to convert calibration chamber to field values, would shift the new curves to the right in Figure 16 and thus even lead to a flatter course.

The diagram with the novel correlation curves is applied in the same way as that in Figure 1 and similar diagrams in the literature. For a soil with a given q_{c1} value, an earthquake causing a cyclic loading with a cyclic stress ratio $CSR = \tau^{\mathrm{ampl}}/\sigma'_{v0}$ lying above the correlation curve will probably lead to liquefaction, while no liquefaction is expected in case of a CSR lying below that curve.

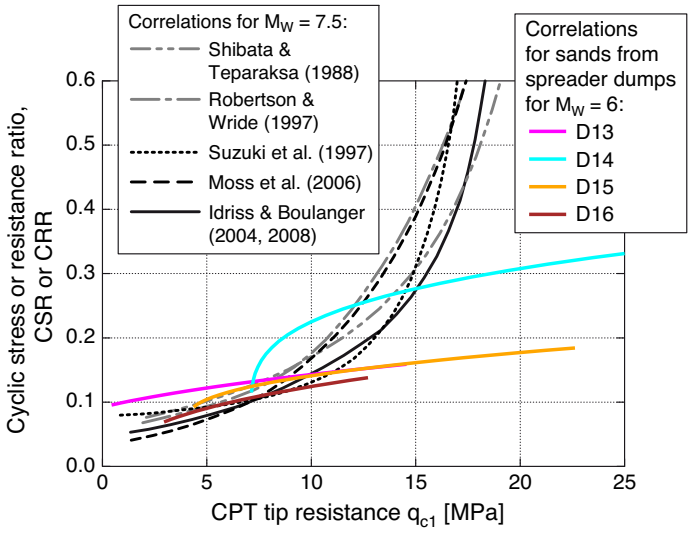

Fig. 16: *Comparison of the $CRR(N_f = 10)$-q_{c1} correlations derived for the four tested sands D13 - D16 with relationships for natural soils and $M_W = 7.5$ from the literature (Idriss & Boulanger [15, 16], after Dobry & Abdoun [9])*

When comparing the novel correlation curves for the soils in the dumps with those available in the literature, it should be kept in mind that the relationships from the literature are valid for an earthquake magnitude $M_W = 7.5$. Applying the formula $MSF = 6.9 \cdot \exp(-M_W/4) - 0.058 \leq 1.8$ proposed by Idriss [14] (see also Boulanger & Idriss [5]),

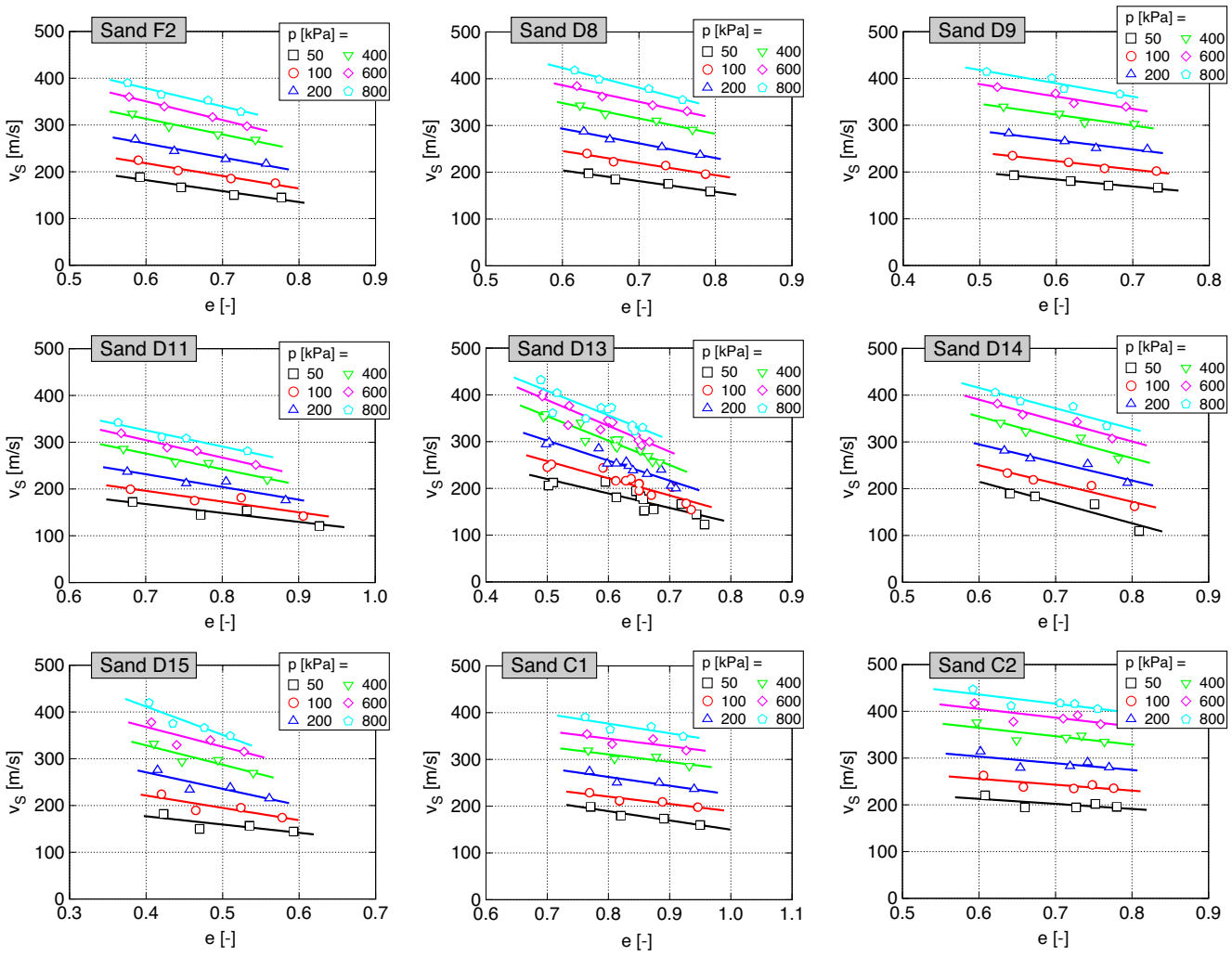

Fig. 17: *Shear wave velocity v_S in dependence of void ratio e and pressure p for all tested materials*

the magnitude scaling factor would be $MSF = 1.48$ for $M_W = 6$. Consequently, the curves for the natural sands in Figure 16 would have to be scaled by this MSF value, i.e. they would be shifted upwards, to obtain curves applicable to earthquakes with $M_W = 6$. In that case most of the novel curves for the dumped soils lay below those for natural soils from the literature. The new correlations for the sands from the spreader dumps do not incorporate any uncertainties regarding a suitable choice of MSF since they were established directly for the number of equivalent cycles $N_{eq} = 10$ being realistic for an earthquake in the Rhenish lignite-mining area.

6 Measurements of shear wave velocity with bender elements

For all ten materials introduced in Section 2 except D16 the shear wave velocity was measured in triaxial samples (diameter 100 mm, height 100 mm). The end plates of the triaxial device were equipped with bender elements. The samples were prepared by moist tamping in eight layers using a degree of undercompaction of 10 %. Afterwards the samples were water-saturated, but no back pressure was applied (i.e. $p' = p$ holds). The effective stress was isotropically increased from $p = 50$ kPa to $p = 800$ kPa in steps Δp of 50 kPa (up to $p = 200$ kPa) or 100 kPa (at $p >$ 200 kPa). At each pressure level the shear wave velocity was measured by means of the bender elements. A single sinusoidal pulse was applied at one end plate. Both the transmitted signal and the signal received at the opposite end plate, after wave propagation through the sample, were recorded at an oscilloscope and later analyzed at a PC. The frequency of the transmitted signal was chosen within the range $8 \leq f \leq 11$ kHz with the aim to receive an output signal that is clearly interpretable. Typical signals for different pressures measured at the same sample are provided in Figure 18. The shear wave velocity $v_S = l_t/t_t$ was calculated with the travel time t_t determined from a comparison of the transmitted and received signals and the length L_t of the travel path which was set equal to the distance of the tips of the bender elements (in accordance with [6, 11]).

In contrast to the calibration chamber tests the samples were tested water-saturated in the present test series with the bender elements in order to allow volume change measurements during the pressure increase via the squeezed out pore water. Preliminary comparative tests on moist and water-saturated samples on a sand with low fines content had demonstrated a negligible effect of the state of saturation on the measured shear wave velocities. The shear wave velocities of the partially saturated samples fell within the

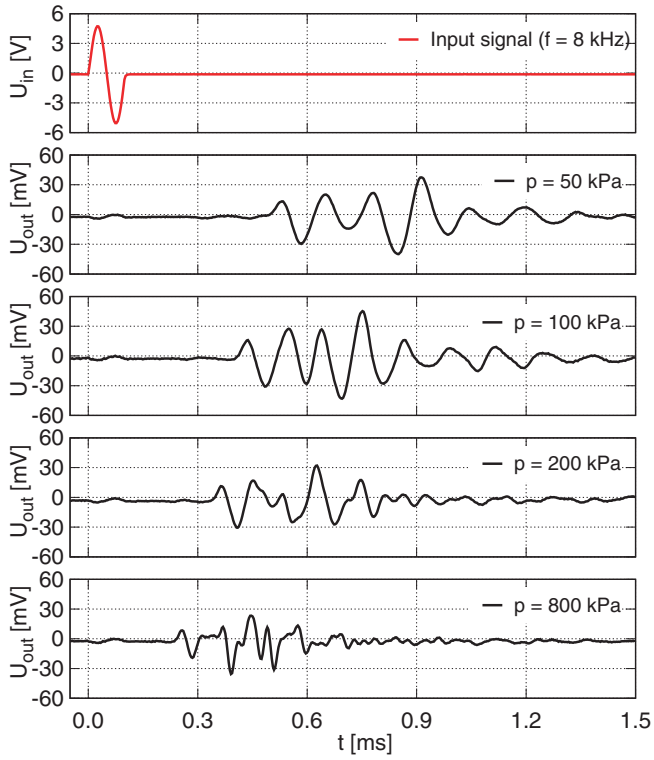

Fig. 18: *Signals received with the bender elements at different pressures on the same sample*

range of scatter of the data for the fully water-saturated samples. The effect of partial saturation on the shear wave velocities could be more pronounced in case of the soils with higher fines content, which will be studied in more detail in future.

For each material several samples with different initial relative densities were tested. Figure 17 collects the diagrams showing the shear wave velocity v_S as a function of void ratio e at different pressures p for all materials. The well-known increase of v_S with decreasing void ratio (i.e. increasing density) and growing pressure is evident in these graphs. The relationship between v_S and e is almost linear for all materials. The diagrams in Figure 19a,b show the well-known underproportional increase of shear wave velocity with pressure for two different initial relative densities $D_{r0} \approx 30$ % and ≈ 60 %.

Figure 20 presents the relationships between the shear wave velocity at a pressure $p = 100$ kPa and relative density D_r for all tested materials. The linear v_S-e curves in Figure 17 are reflected in the linear v_S-D_r relationships in Figure 20. For each material the v_S values for relative densities of 30 % and 60 % have been read out of the linear curves in Figure 20 and plotted versus the parameters of the grain size distribution curve in Figure 21. The diagrams show only weak trends for a decrease of v_S with fines content FC and an increase with mean grain size d_{50}, while the effect of C_u is small.

For the evaluation of field data, again a function for the pressure-normalization of v_s is necessary. In order to derive such function, the $v_S(p)$ data for a certain material shown in Figure 19a,b has been fitted by the power law

$$v_S = a \cdot p^b \tag{4}$$

with two material constants a and b, resulting in the continuous curves presented in Figure 19a,b. These curves have been used afterwards to determine the shear wave velocity v_S at $p = 100$ kPa, denoted v_{S1}. The $v_S(p)$ data from Figure 19a,b have then been divided by v_{S1}, resulting in the curves $v_S(p)/v_{S1}$ collected in the diagrams of Figure 19c,d. Of course $v_S/v_{S1} = 1$ has to be fulfilled at $p = 100$ kPa. Obviously, the v_S/v_{S1} data for a certain relative density fall together in an almost unique curve. Furthermore, the average curves $v_S(p)/v_{S1}$ for $D_{r0} = 30$ % and 60 % do not differ much. Therefore, they can be described by a unique function (dashed curve in Figure 19c,d):

$$\frac{v_S}{v_{S1}} = \frac{1}{C_{vs}} = \left(\frac{p}{100}\right)^c \tag{5}$$

with the parameter $c = 0.28$. A presentation analogously to Eq. (2) reads:

$$v_{S1} = C_{vs}\, v_S \tag{6}$$

7 Correlation between shear wave velocity and liquefaction resistance

The correlations between the liquefaction resistance $CRR(N_f = 10)$ and the shear wave velocity v_{S1} for $p = 100$ kPa are established in the same way as the $CRR(N_f = 10)$-q_{c1} correlations. The procedure is shown for the material D13 in Figure 22, where the v_{S1}-D_r relationship from Figure 20 ($v_S = v_{S1}$ because of $p = 100$ kPa) replaces the q_{c1}-D_r diagram used in Figure 15. The resulting correlation between $CRR(N_f = 10)$ and v_{S1} in Figure 22c has a linear shape, since both relationships $CRR(N_f = 10)$-D_r and v_{S1}-D_r had been approximated by linear curves.

The same applies to the $CRR(N_f = 10)$-v_{S1} relationships derived for the other tested materials. They are collected in Figure 23. The relative position of the $CRR(N_f = 10)$-v_{S1} relationships of the different materials approximately agrees with that of the $CRR(N_f = 10)$-D_r curves in Figure 7. Materials with a higher fines content and a lower mean grain size tend to possess a lower liquefaction resistance. The new correlations for the sands from the dumps mostly lie below the CRR-v_{S1} relationship for natural sands with different amount of fines according to Andrus & Stokoe [3], but slightly above the bounding curve for uncompacted recent artificial fills proposed by Dobry et al. [10] (Figure 23).

It has to be considered, however, that the CRR-v_{S1} relationships of Andrus & Stokoe [3] and Dobry et al. [10] have been developed for $M_W = 7.5$. Using the equation for the magnitude scaling factor $MSF = (M_W/7.5)^{-2.56}$ given in Figure 2, a value of $MSF = 1.77$ is obtained for $M_W = 6$. The curves for $M_W = 7.5$ would have to be scaled by this MSF value to obtain relationships applicable for $M_W = 6$. If such scaling is done, the CRR-v_{S1} curves of the new correlations for the sands from the spreader dumps would lie below the respective relationships based on real seismic events from the literature.

8 Summary, conclusions and outlook

Correlations between the liquefaction resistance of sands from spreader dumps of opencast mines in the Rhenish lignite-mining area with both the CPT tip resistance q_c and the shear wave velocity v_S have been developed based on an extensive laboratory testing program. Eight materials from

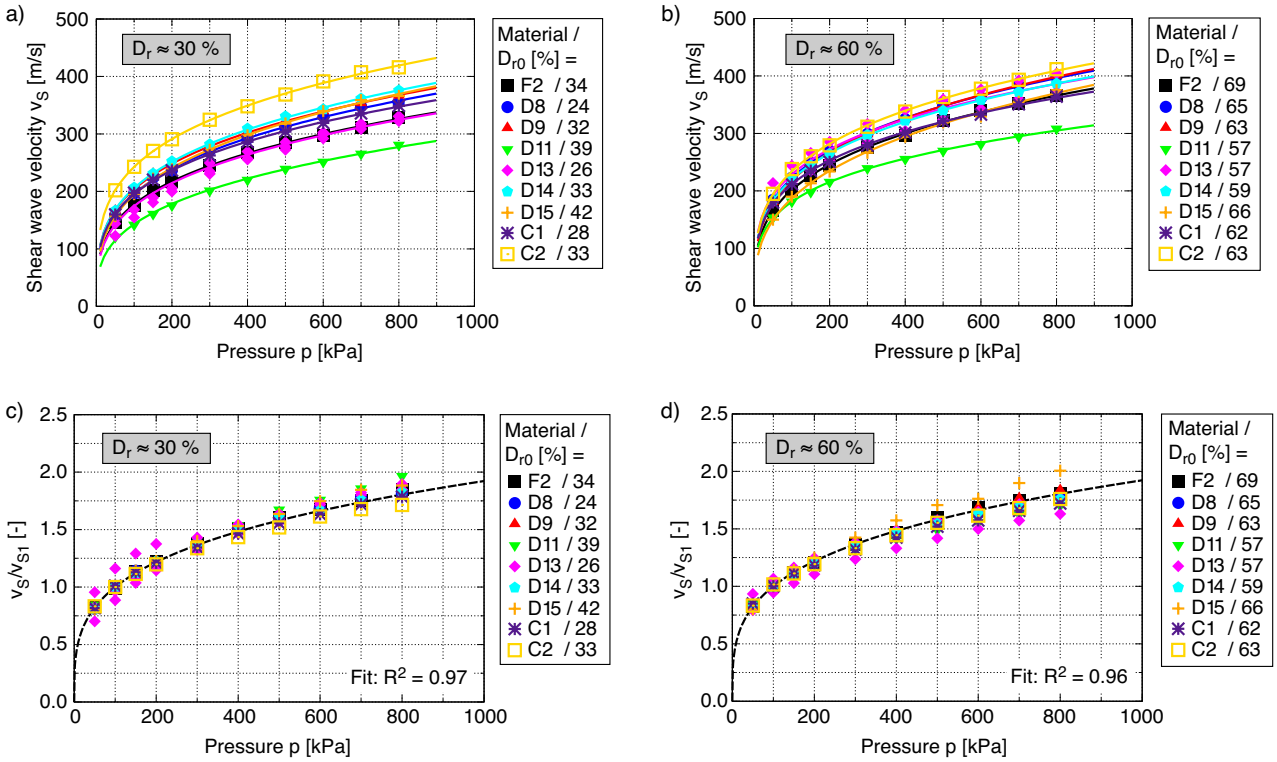

Fig. 19: a),b) *Dependence of shear wave velocity v_S on pressure p for initial relative densities $D_{r0} \approx 30$ % or 60 %, respectively. c),d) Same data in a representation with v_S/v_{S1} versus p, with $v_{S1} = v_S(p = 100\ kPa)$ on the ordinate.*

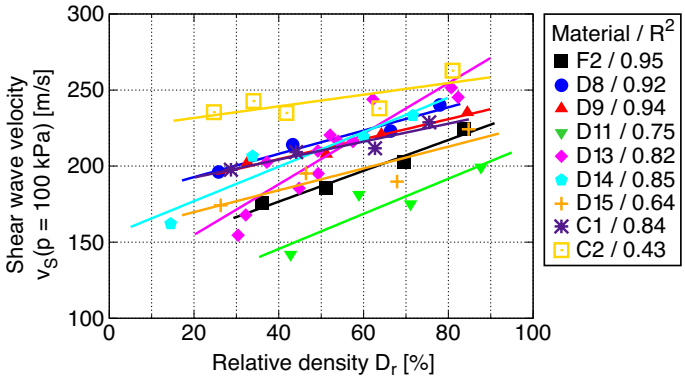

Fig. 20: *Shear wave velocity v_S for $p = 100$ kPa as a function of relative density D_r for all tested materials*

the dumps and two standard sands of the IBF were used for the experimental investigation. The liquefaction resistance $CRR(N_f = 10)$ necessary to cause a failure (10 % axial strain) in 10 cycles was determined in undrained cyclic triaxial tests on samples prepared with different densities and loaded by different amplitudes. The CPT tip resistance was determined from soundings in a calibration chamber, while the shear wave velocity was measured in triaxial samples by means of bender elements. Both quantities q_c and v_S were obtained for different combinations of pressure and density. Based on the data correlations between $CRR(N_f = 10)$ and the q_c and v_S values for a pressure $p = 100$ kPa (i.e. for q_{c1} and v_{S1}) were developed. Furthermore, equations for the pressure-normalization of q_c and v_S have been derived, which are necessary for the analysis of field test data.

The $CRR(N_f = 10)$-q_{c1} correlations of three of the four tested materials almost coincide, while the material with the lowest fines content and the steepest grain size distribution curve shows significantly larger $CRR(N_f = 10)$ values for the same q_{c1}. The $CRR(N_f = 10)$-q_{c1} relationships of the sands from the spreader dumps run flatter than those derived for natural sands in the literature and they do not show the strong overproportional increase at larger values of tip resistance which is evident in the available correlation diagrams for natural soils.

The nine $CRR(N_f = 10)$-v_{S1} correlations established so far all show a linear shape. For a certain value of v_{S1} the liquefaction resistance $CRR(N_f = 10)$ read from the correlations depends on the grain size distribution curve of the material. The relative position of the correlation curves in the $CRR(N_f = 10)$-v_{S1} diagram shows the same trends as the $CRR(N_f = 10)$-D_r relationships derived from the undrained cyclic triaxial tests. Materials with a higher fines content and a lower mean grain size tend to possess a lower liquefaction resistance.

In future, the dependencies of the $CRR(N_f = 10)$-q_{c1} and the $CRR(N_f = 10)$-v_{S1} correlations on grain size distribution curve will be further inspected based on additional experimental data collected for several other sands from the dumps with various grain size distribution curves. Such dependence on the grain size distribution curve would mean that one also needs general information about the granulometric composition of the sands in the dumps in order to select a suitable correlation curve. CPT soundings and measurements of the shear wave velocity (e.g. by means of a seismic CPT) would thus have to be accompanied by exemplary drillings in order to obtain disturbed sand samples for further classification in the laboratory.

Furthermore, up to now only isotropic states of stress

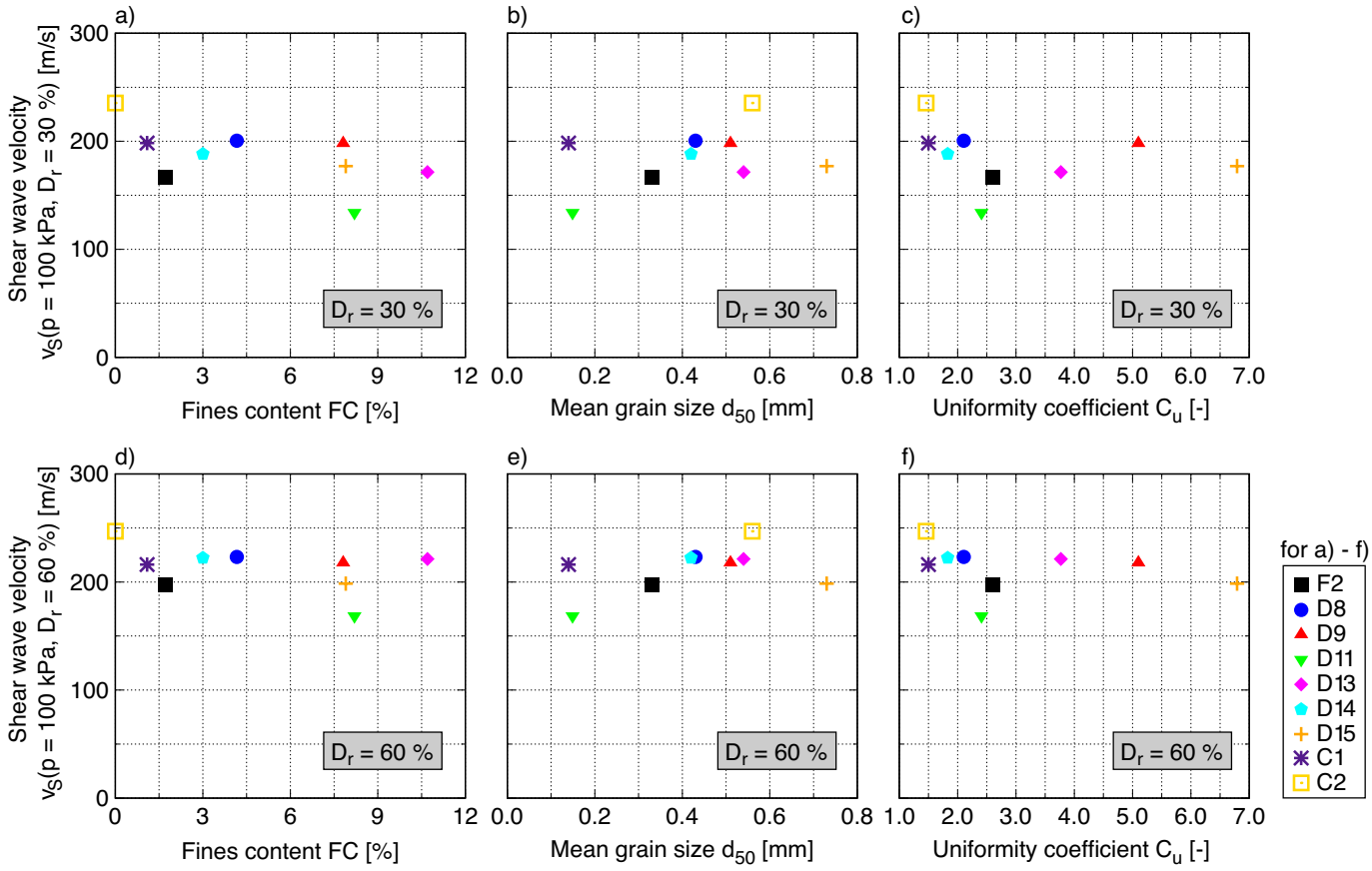

Fig. 21: *Shear wave velocity v_S for p = 100 kPa and a-c) D_r = 30 % or d-f) D_r = 60 % in dependence of fines content FC, mean grain size d_{50} and uniformity coefficient C_u*

have been investigated. The effect of stress anisotropy on the $CRR(N_f = 10)$-q_{c1} and the $CRR(N_f = 10)$-v_{S1} relationships will be another issue of further research.

Since the $CRR(N_f = 10)$-q_{c1} and $CRR(N_f = 10)$-v_{S1} correlations for a certain material proposed in this paper have been derived from laboratory data for the same relative density in all three types of tests, both types of correlations should deliver the same liquefaction resistance if applied to real test data. In future the equivalence of both correlations will be checked in a field campaign, where various quantities (amongst others q_c and v_S) are measured and undisturbed samples are taken for the determination of the liquefaction resistance in the laboratory.

In the undrained cyclic triaxial tests the loading has been started directly after sample preparation, the application of the initial effective stress and a resting time of about 1 h to wait for sample deformations. The same applies to the measurements of q_c and v_S in the calibration chamber or with the bender elements. Therefore, aging effects which may increase all three quantities, $CRR(N_f = 10)$, q_c and v_S, with time, and their possible influence on the correlation curves have not been studied yet. This will be a matter of future research.

The development of a correction factor K_{cc} for the conversion of $q_c = q_{c,Chamber}$ values measured in the calibration chamber to $q_{c,Field}$ values to be expected in the field will be another topic of future research. For that purpose, soundings in calibration chambers with different diameters will be performed.

References

[1] *DIN 4094-1:2002. Baugrund - Felduntersuchungen - Teil 1: Drucksondierungen*, 2002.

[2] L. Ahorner. Abschätzung der statistischen Wiederkehrperiode von starken Erdbeben im Gebiet von Köln auf Grund von geologisch-tektonischen Beobachtungen an aktiven Störungen. In *Mitteilungen der Deutschen Geophysikalischen Gesellschaft*, volume 2, pages 2–9, 2001.

[3] R.D. Andrus and K.H. Stokoe II. Liquefaction resistance of soils from shear-wave velocity. *Journal of Geotechnical and Geoenvironmental Engineering, ASCE*, 126(11):1015–1025, 2000.

[4] R.W. Boulanger and I.M. Idriss. Probabilistic standard penetration test-based liquefaction-triggering procedure. *Journal of Geotechnical and Geoenvironmental Engineering, ASCE*, 138(10):1185–1195, 2012.

[5] R.W. Boulanger and I.M. Idriss. CPT and SPT based liquefaction triggering procedures. Technical Report UCD/CGM-14/01, Center for Geotechnical Modeling, University of California at Davis, 2014.

[6] G.M. Brignoli, M. Gotti, and K.H. II. Stokoe. Measurement of shear waves in laboratory specimens by means of piezoelectric transducers. *Geotechnical Testing Journal, ASTM*, 19(4):384–397, 1996.

[7] T. Camelbeeck, T. vanEck, R. Pelzing, L. Ahorner, L. Loohuis, H.W. Haak, P. Hoang-Trong, and D. Hollnack. The 1992 Roermond earthquake, the Netherlands, and its aftershocks. *Geologie en Mijnbouw*, 73:181–197, 1994.

[8] R.O. Cudmani. Statische, alternierende und dynamische Penetration in nichtbindige Böden. Dissertation,

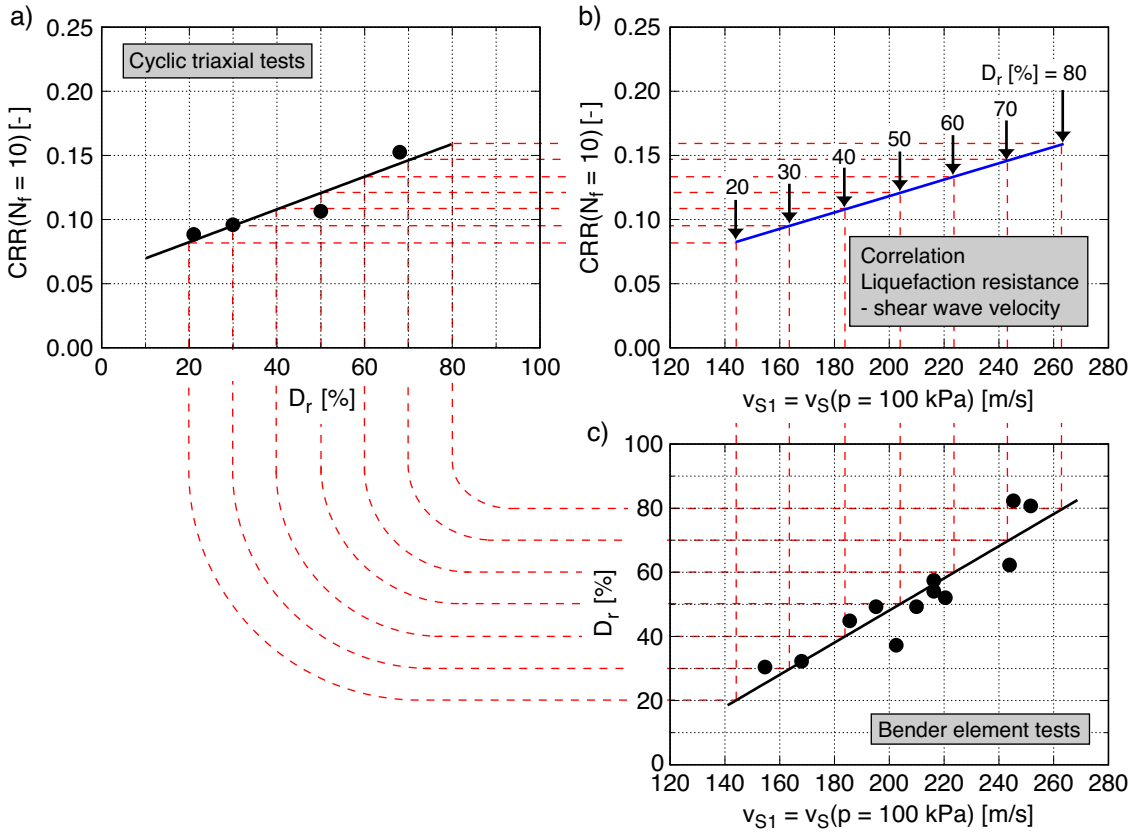

Fig. 22: *Development of the correlation diagram between shear wave velocity v_{S1} for $p = 100$ kPa and liquefaction resistance $CRR(N_f = 10)$ for material D13*

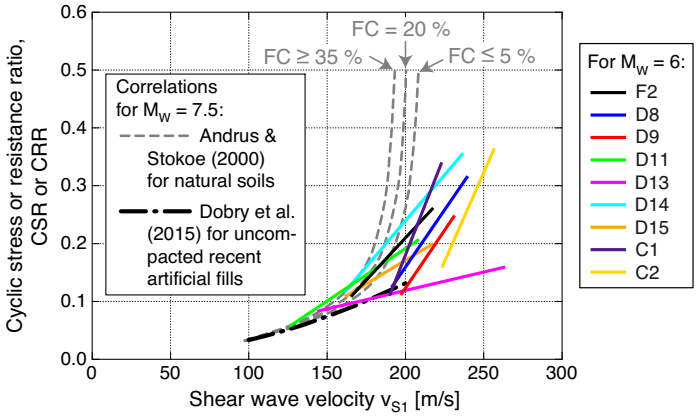

Fig. 23: *Comparison of the $CRR(N_f = 10)$-v_{S1} correlations derived for the nine tested materials with respective relationships for natural soils (Andrus & Stokoe [3], cf. Figure 2) or uncompacted recent artificial fills (Dobry et al. [10], cf. Figure 3) from the literature*

Veröffentlichungen des Institutes für Bodenmechanik und Felsmechanik der Universität Fridericiana in Karlsruhe, Heft 152, 2001.

[9] R. Dobry and T. Abdoun. 3rd Ishihara Lecture: An investigation into why liquefaction charts work: A necessary step toward integrating the states of art and practice. *Soil Dynamics and Earthquake Engineering*, 68:40–56, 2015.

[10] R. Dobry, T. Abdoun, K.H. Stokoe II, R.E.S. Moss, M. Hatton, and H. El Ganainy. Liquefaction potential of recent fills versus natural sands located in high-seismicity regions using shear-wave velocity. *Journal of Geotechnical and Geoenvironmental Engineering, ASCE*, 141, 2015.

[11] R. Dyvik and C. Madshus. Laboratory measurements of G_{max} using bender elements. In *Proceedings, ASCE Annual Convention: Advances in the Art of Testing Soils Under Cyclic Conditions, Detroit, Michigan*, pages 186–196, 1985.

[12] K.-G. Hinzen. The use of engineering seismological models to interpret archaeoseismological findings in Tolbiacum, Germany, a case study. *Bulletin of the Seismological Society of America*, 95:521–539, 2005.

[13] K.-G. Hinzen and S.K. Reamer. Seismicity, seismotectonics, and seismic hazard in the northern Rhine area. In S. Stein and S. Mazzotti, editors, *Continental Intraplate Earthquakes: Science, Hazard, and Policy Issues: Geological Society of America Special Paper 425*, pages 225–242, 2007.

[14] I. M. Idriss. An update to the Seed-Idriss simplified procedure for evaluating liquefaction potential. In *Proceedings, TRB Workshop on New Approaches to Liquefaction, Publication No. FHWARD-99-165, Federal Highway Administration*, 1999.

[15] I.M. Idriss and R.W. Boulanger. Semi-empirical procedures for evaluating liquefaction potential during earthquakes. In D. Doolin, A. Kammerer, T. Nogami, R.B. Seed, and I. Towhata, editors, *Proceedings of the 3rd International Conference on Earthquake Geotechnical Engineering, University of California, Berkeley*, volume 1, pages 32–56, 2004.

[16] I.M. Idriss and R.W. Boulanger. Soil liquefaction during earthquakes. Technical Report MNO-12, Earthquake Engineering Research Institute, Oakland, CA, 2008.

[17] K. Ishihara. *Soil Behaviour in Earthquake Geotechnics*. Oxford Science Publications, 1996.

[18] C.H. Juang, J. Ching, C.-S. Ku, and Y.-H. Hsieh. Unified CPTu-based probabilistic model for assessing probability of liquefaction of sand and clay. *Géotechnique*, 62(10):877–892, 2012.

[19] R. Kayen, R.E.S. Moss, E.M. Thompson, R.B. Seed, K.O. Cetin, A. Der Kiureghian, Y. Tanaka, and K. Tokimatsu. Shear-wave velocity-based probabilistic and deterministic assessment of seismic soil liquefaction potential. *Journal of Geotechnical and Geoenvironmental Engineering, ASCE*, 139:407–419, 2013.

[20] R.S. Ladd. Preparing test specimens using undercompaction. *Geotechnical Testing Journal, ASTM*, 1(1):16–23, 1978.

[21] P.W. Mayne and H. Kulhawy. Calibration chamber database and boundary effects correction for CPT data. In A.-B. Huang, editor, *Calibration chamber testing*, pages 257–264. Elsevier, 1991.

[22] R. E. S. Moss, R. B. Seed, R. E. Kayen, J. P. Stewart, T. L. Youd, and K. Tokimatsu. Field case histories for CPT-based in situ liquefaction potential evaluation.Geoengineering Research Rep. UCB/GE-2003/04. Technical report, , 2003.

[23] R.E.S. Moss, R.B. Seed, R.E. Kayen, J.P. Stewart, A. Der Kiureghian, and K.O. Cetin. CPT-based probabilistic and deterministic assessment of in situ seismic soil liquefaction potential. *Journal of Geotechnical and Geoenvironmental Engineering, ASCE*, 132(8):1032–1051, 2006.

[24] V. Osinov and R. Cudmani. Theoretical investigation of the cavity expansion problem based on a hypoplasticity model. *International Journal For Numerical And Analytical Methods in Geomechanics*, 25(5):473–495, 2001.

[25] R. Petri, W. Stein, D. Dahmen, and K. Buschhüter. Sustainable follow-up use of recultivated surfaces. Evaluation of residual lakes and high dumps in the Rhenish lignite-mining area after the end of mining supervison. *World of Mining*, 65(2):92–101, 2013.

[26] P. K. Robertson and C. E. Wride. Cyclic liquefaction and its evaluation based on SPT and CPT. In *Proceedings, NCEER Workshop on Evaluation of Liquefaction Resistance of Soils*, 1997.

[27] P.K. Robertson and R.G. Campanella. Liquefaction potential of sands using the CPT. *Journal of Geotechnical Engineering, ASCE*, 111(3):384–403, 1985.

[28] P.K. Robertson, D.J. Woeller, and W.D.L. Finn. Seismic cone penetration test for evaluating liquefaction potential under cyclic loading. *Canadian Geotechnical Journal*, 29(4):686–695, 1992.

[29] P.K. Robertson and C.E. Wride. Evaluating cyclic liquefaction potential using the cone penetration test. *Canadian Geotechnical Journal*, 35:442–459, 1998.

[30] H.B. Seed, I.M. Idriss, and I. Arango. Evaluation of liquefaction potential using field performance data. *Journal of Geotechnical Engineering, ASCE*, 109(3):458–482, 1983.

[31] T. Shibata and W. Teparaksa. Evaluation of liquefaction potential of soils using cone penetration tests. *Soils and Foundations*, 28(2):49–60, 1988.

[32] Y. Suzuki, K. Koyamada, and K. Tokimatsu. Prediction of liquefaction resistance based on CPT tip resistance and sleeve friction. In *Proceedings, 14th International Conference on Soil Mechanics and Foundation Engineering, Hamburg, Germany*, volume 1, pages 603–606, 1997.

[33] F. Tatsuoka, K. Ochi, S. Fujii, and M. Okamoto. Cyclic undrained triaxial and torsional shear strength of sands for different sample preparation methods. *Soils and Foundations*, 26(3):23–41, 1986.

[34] K. Tokimatsu and A. Uchida. Correlation between liquefaction resistance and shear wave velocity. *Soils and Foundations*, 30(2):33–42, 1990.

[35] T. Wichtmann, K. Steller, Th. Triantafyllidis, M. Back, and D. Dahmen. An experimental parametric study on the liquefaction resistance of sands in spreader dumps of lignite opencast mines. *Soil Dynamics and Earthquake Engineering*, 2019.